Applied Thermal Engineering 210 (2022) 118339

Contents lists available at ScienceDirect

Applied Thermal Engineering

journal homepage: www.elsevier.com/locate/apthermeng

Research Paper

High performance, microarchitected, compact heat exchanger enabled by 3D printing

Tisha Dixit [a,1], Ebrahim Al-Hajri [a], Manosh C Paul [b], Perumal Nithiarasu [c], S. Kumar [b,d,*]

[a] Department of Mechanical Engineering, Khalifa University, Abu Dhabi, United Arab Emirates
[b] Systems, Power & Energy Research Division, James Watt School of Engineering, University of Glasgow, Glasgow G12 8LT, United Kingdom
[c] Zienkiewicz Centre for Computational Engineering, Faculty of Science and Engineering, Swansea University, Swansea, United Kingdom
[d] Glasgow Computational Engineering Centre, University of Glasgow, Glasgow G12 8LT, United Kingdom

ARTICLE INFO

Keywords:
Additive manufacturing
Triply periodic minimal surfaces
Schoen's gyroid lattice
Architected materials
Heat exhanger

ABSTRACT

Additive manufacturing has created a paradigm shift in materials design and innovation, providing avenues and opportunities for geometric design freedom and customizations. Here, we report a microarchitected gyroid lattice liquid–liquid compact heat exchanger realized via stereolithography additive manufacturing as a single ready-to-use unit. This lightweight (~240 kg/m^3) compact heat exchanger (with conjoined headers), with an engineered porosity of 80% and a separating wall thickness of 300 μm, has a surface to volume ratio of 670 m^2/m^3. X-ray computed tomography imaging confirms a defect-free 3D printed heat exchanger. The thermo-hydraulic characteristics were experimentally measured using water as the working fluid. The measurements indicate that the heat exchanger evinces an overall heat transfer coefficient of $120-160 W/m^2K$ for hot fluid Reynolds number Re_h in the range of $10-40$. Additionally, finite element analysis was conducted to evaluate the thermo-hydraulic characteristics of the gyroid lattice heat exchanger. The experimental results show -a 55% increase in exchanger effectiveness for the additively manufactured gyroid lattice heat exchanger in comparison to a thermodynamically equivalent, most-efficient, counter-flow heat exchanger at one tenth of its size. The superiority of our architected heat exchanger to extant work is also demonstrated.

1. Introduction

Additive manufacturing enables realization of complex three-dimensional (3D) geometries from a digital file with a range of materials. Additive manufacturing (AM), commercially known as 3D printing, encompasses a comprehensive set of processes including, fused filament fabrication (FFF) [1], stereolithography (SLA) [2], binder jetting (BJ) [3], multijet fusion (MJF) [4], material jetting (MJ) [5], selective laser sintering (SLS) [6], selective laser melting (SLM) [7] and electron beam melting [8], to name a few. Emerging advances in AM enable creation of material architectures even at micro- and nano-scales [9,10] providing flexibility and opportunities to tackle manufacturing challenges.

AM offers enormous scope for product design and innovation. Heat exchanger (HX) is a functional component of a thermal system which facilitates a positive/negative temperature gradient via directional flow of heat energy through either thermally conductive wall, energy storage matrix, fluid interface or two-phase heat transfer. The complex geometrical designs of HXs are often limited by the constraints of conventional manufacturing techniques. The mounting demands for lightweight engineering and miniaturization have further accelerated AM-enabled new designs of compact HXs which perform at par, if not better than the traditional counterparts [11,12]. Emergence of AM as a manufacturing tool has gained momentum in the manufacture of thermal systems such as oscillating heat pipe [13], manifold microchannel [14,15], louvered plate-fin [16,17], double corrugated tube-in-shell [18], transpiration cooling porous plates with partition walls [19] and finned tube [20] HXs. These HXs have been fabricated using different materials such as titanium alloys [13,14], stainless steel [14,20], aluminium alloy [14,17,18] and Inconel [15], mostly via SLM technique focusing on power plant cooling [14] and aerospace applications [17].

In the pursuit of lightweight engineering, there is a constant hunt for ultra-lightweight materials featuring high performance. Advances in

* Corresponding author at: Materials and Manufacturing Research Group, James Watt School of Engineering, University of Glasgow, Glasgow G12 8LT, United Kingdom.
E-mail address: s.kumar@eng.oxon.org (S. Kumar).
[1] Université Paris-Saclay, CEA, Département des Accélérateurs, de la Cryogénie et du Magnétisme, 91191, Gif-sur-Yvette, France.

https://doi.org/10.1016/j.applthermaleng.2022.118339
Received 16 June 2021; Received in revised form 27 February 2022; Accepted 10 March 2022
Available online 18 March 2022

Nomenclature

A_c	Cross-sectional area at the inlet (m^2)
A_s	Heat exchange surface area (m^2)
C_p	Specific heat of the fluid ($J/kg.K$)
D_h	Hydraulic diameter (m)
$\dot{m}$	Mass flow rate (kg/s)
NTU	Number of heat transfer units
Q	Heat transfer (W)
U	Heat transfer coefficient (W/m^{2}K)
T	Temperature (K)
ΔT_{LMTD}	Log mean temperature difference of the fluids (K) defined by Eq. (4)
$\dot{V}$	Volumetric flow rate (m^3/s)
V	Heat exchanger core volume (m^3)

Subscripts

c	Cold fluid
h	Hot fluid
i	Inlet
o	Outlet
min	Minimum

Greek letters

μ	Dynamic viscosity of fluid ($N.s/m^2$)
$\varnothing$	Porosity
$\overline{\rho}$	Relative density
ε	Heat exchanger effectiveness

AM-enabled architected cellular materials [21,22] with tunable mechanical [2,23–25], sensing [26,27], electromagnetic shielding [28], optical [29], energy storage [30], and thermal [31–33] properties are realized by the virtue of tailored topological design [34,35] at different length scales. Several AM-enabled periodic cellular architectures [9] such as honeycombs, tetrahedral, octahedral, octet, Kelvin-cell, truss-lattices, plate-lattices and triply periodic minimal surface (TPMS) lattices are extensively being explored for both structural and/or functional attributes in lightweight applications, energy absorbing structures, thermal management systems and bio-scaffolds [22]. 3D printed lattice-cores of single-phase/two-phase HXs with tetrahedral lattice frame [36,37], hollow tube lattices [38], TPMS-lattice [39], octet-truss [40] and rotated cubic lattice-architectures [41] have been explored for use in bi-continuous fluid networks [38], membrane devices [39], aerospace thermal control [37], electronic cooling [40] and solar receivers [41].

The performance characteristics of AM-enabled architected HXs are governed by the choice of material, cellular geometry and the characteristic length scale of the structured topology. These choices also limit the choice of AM technique and in turn the smallest geometrical features that can be realized for architected HXs. The performance and effectiveness of HX is governed by the material's thermal conductivity, fluid separating wall thickness and the heat exchange surface area. Metals due to their high thermal conductivity are the most preferred candidates for heat exchangers [42]. However, to realize lightweight, cost-effective HXs capable of exhibiting enhanced fouling and corrosion resistance for low temperature working fluids, polymer and polymer composites are considered [43–47]. Studies on polymer and polymer composite HXs show that hollow fibre [48–52], cross-corrugated film [53], sheet [54], shell and tube [46] and finned tube [55] HXs have been explored for use in fuel cells [53], refrigeration [43], low-temperature heat recovery systems [46,55], automotive radiators [50] and desalination processes [52]. The undesirable effect of low thermal conductivity of polymer can be overcome with thin-walled HXs but we must ensure structural integrity of fluid separating walls under fluid flow. Fortunately, AM-enabled metamaterials (micro- and/or nano-architected lattices) can mitigate the low mechanical strength barrier of polymers [9] such that re-distribution of load can be optimally achieved by the metamaterial architecture in addition to light-weighting the compact HX cores.

Triply periodic minimal surface (TPMS) architectures have been demonstrated as a suitable choice for scaffolds owing to their tailorable mechanical and functional characteristics [56–58]. Recently, the thermal [59], electrical [60], fluid flow [61] and heat exchange [62–64] characteristics of different TPMS architectures have been explored. The smooth inter-connected pores within the TPMS geometry provides a large heat exchange surface area making it a suitable candidate for heat exchangers [65,66]. A very few studies have investigated TPMS-based lattices for heat exchange applications thus far. Peng et al. [62] conducted computational study on TPMS HX and concluded from their numerical results that the heat transfer capability of TPMS HX is 7.5 times more than that of a traditional plate HX. Another computational study performed by Li et al. [63] with the aim of employing TPMS HX to enhance the efficiency of supercritical CO_2 Brayton cycle showed numerically that gyroid and Schwarz-D HXs improve the thermal performance by 15–100% compared to printed-circuit HX. An actual prototype for TPMS based HXs has been successfully 3D printed and experimentally tested by Kim and Yoo [64] with a channel wall thickness a of 900μm.

In this study, we report the heat exchange performance of a lightweight, gyroid lattice, next-generation compact heat exchanger. The gyroid is a triply periodic minimal surface (with zero mean curvature) geometry and was identified by Alan Schoen in 1970 [75]. Novel microarchitected Schoen's gyroid is chosen as non-conventional extended surface for the heat exchanger core. The advantage of such architected geometry is the freedom to tailor its scale-dependent properties. Accordingly, a liquid–liquid gyroid lattice HX made of polymer with an engineered porosity of 80% was realized via additive manufacturing. Such microarchitected HX possesses a compactness of 670m^2/m^3 and a wall thickness as thin as 300μm. The heat exchanger core weighs just ~8g. Presently, the complex 3D geometry of gyroid architecture can only be fabricated via additive manufacturing. Furthermore, in conventional manufacturing, the heat exchanger core and the inlet and outlet flow directional headers are to be separately fabricated and later joined as these can't be produced together in one go. Utilizing AM technology, we realized polymer exchanger headers and connecting pipes as a single unit along with the core in form of a ready-to-use heat exchanger having a total weight of ~50g (~240 kg/m^3). The thermo-hydraulic performance of micro-architected gyroid lattice, compact heat exchanger is evaluated both experimentally and computationally. The gyroid lattice heat exchanger exhibits a 55% increase in effectiveness in comparison to a thermodynamically equivalent, most-efficient, counter-flow HX at 1/10th of its size.

2. Materials & methods

i. Design of gyroid architecture. Schoen's gyroid structure forms a subset of the triply periodic minimal surfaces that are known to have non-self-intersecting and highly symmetrical periodic surfaces [67,68]. It partitions an enclosed volume into two identical helical spaces described by the equation: $cosxsiny + cosysinz + coszsinx = C$ [69]. Construction of the complex gyroid structure from a frame of curves to form continuously filled surfaces is progressively done using the 3D CAD SolidWorks^{TM} design tool (Fig. 1a). The porosity of the gyroid lattice structure is kept at 80%. Alternatively, the relative density of the gyroid

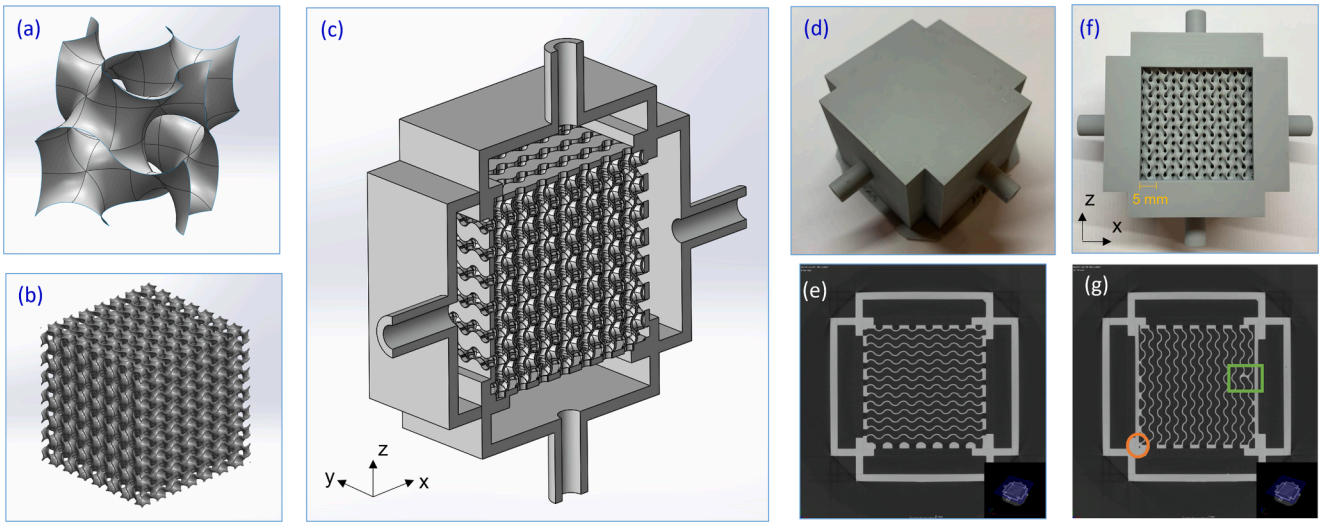

Fig. 1. Design and fabrication of gyroid lattice compact heat exchanger (a) CAD surface model of the gyroid unit cell of $4.6mm \times 4.6mm \times 4.6mm$ (b) CAD model of gyroid lattice exchanger core comprising $7 \times 7 \times 7$ array of gyroid unit cells with a wall thickness of $300\mu m$ and 80% porosity (c) CAD sectional view of the heat exchanger clearly depicting the gyroid core, covering plates and headers assembly (d) 3D printed heat exchanger (e) X-ray micro-computed tomographic image of a plane passing through the mid-height of the heat exchanger and (f) 3D printed heat exchanger without cover plate (g) small scale imperfections.

structure (fraction of solid in the lattice), $\bar{\rho} = (1 - \varnothing) = 20\%$. The smallest dimension that could be flawlessly printed with an Asiga SLA 3D printer is 300μm and therefore the wall thickness - the smallest geometric feature of the gyroid structure is kept at 300μm. The prescribed wall thickness and the porosity $\varnothing = 80\%$, yield a unit cell size of 4.6mm (Fig. 1b) resulting in a surface area density (compactness) of $670\text{m}^2/\text{m}^3$. This makes the designed Schoen's gyroid structure well-suited for liquid–liquid compact heat exchangers as it exhibits a surface area to volume ratio $S/V > 400\text{m}^2/\text{m}^3$.

ii. 3D printing via stereolithography. The gyroid lattice structure is realized via an upside-down SLA additive manufacturing technique using ASIGA PRO2™ 75 desktop 3D printer. PlasGRAY V2 photopolymer resin was used for fabricating the gyroid structure. Considering the maximum build envelope of the 3D printer, the exchanger core comprising an array of $7 \times 7 \times 7$ unit cells was chosen (Fig. 1c). Owing to the three-dimensional periodicity of gyroid lattice structure, the exchanger core forms two identical conduits for channelizing the flow of two separate fluids. When fluids flow through these passages, heat exchange between the fluids takes place as they are in thermal communication with one another. Right closure of passages with covering plates on four sides of the core, with remaining two sides being completely sealed, creates inlet and outlet channels for two fluids. The fluid distribution and collection at the entry and exit of the exchanger core is enabled by rectangular headers which have circular protrusions for pipe connections (Fig. 1d). These protrusions also facilitate cleansing out any liquid resin trapped inside the heat exchanger using isopropanol solution during the post-processing of the heat exchanger after 3D printing. The heat exchanger is thereafter air-dried and cured by ultraviolet light rays. The entire assembly of the exchanger core, covering plates and headers with an overall dimension of $76.2mm \times 76.2mm \times 36.2mm$ is fabricated as a single unit – a feat achievable by ASIGA PRO2™ 75 desktop DLP 3D printer (Build volume $144 \times 81 \times 200mm$; layer resolution $75\mu m$; slice thickness $50\mu m$; positioning precision $1\ \mu m$). The time taken to 3D print this assembly is approximately 9 h and it weighs $\sim 50g$. X-ray micro-computed tomographic image of a plane passing through the mid-height of 3D printed heat exchanger is shown in Fig. 1e and the 3D printed heat exchanger without cover plate is shown in Fig. 1f. Some of the important geometrical parameters of the 3D printed gyroid heat exchanger are summarized in Table 1.

iii. X-ray CT imaging. Since the wall thickness of the gyroid structure is kept at 300 μm, it is important to ensure that the fluid separating walls are defect-free to prevent leakage of fluids. Moreover, in practice, additively manufactured gyroid lattices may have process induced defects depending upon the AM technique employed and the scale of the geometry being produced. As the heat-exchanger was 3D printed as a single ready-to-use enclosed unit, visual inspection of the gyroid structure is out of scope. The defect-structure of the exchanger is therefore assessed via three-dimensional computed tomography using the 'Phoenix Nanotom®m X-ray NanoCT® System'. The digital 3D replica and 2D radiographs are manually scrutinized to capture the presence of any holes in the exchanger walls which might lead to leakage of fluids. It is affirmed that there exist no defects in the separating walls eliminating the likelihood of inter-mixing between the two exchanger fluids (Fig. 1e). However, small scale imperfections are observed as shown in Fig. 1g.

Table 1
Geometrical properties of 3D printed gyroid lattice compact heat exchanger.

Parameters	Values
Surface area density (heat transfer surface area on one side to the total volume)	$670m^2/m^3$
Relative density $\bar{\rho}$ (porosity,$\varnothing$)	20% (80%)
Unit cell size	$4.6mm \times 4.6mm \times 4.6mm$
Wall thickness of gyroid structure	$300\mu m$
Array of unit cells	$7 \times 7 \times 7$
Exchanger core overall dimension	$32.2mm \times 32.2mm \times 32.2mm$
Heat transfer surface area on one side	$0.0223m^2$
Hydraulic diameter	$2.3934mm$

iv. Heat transfer characterization. The practical utility of the gyroid compact heat exchanger can be evaluated by assessing its heat transfer characteristics. A table-top test rig was developed for this purpose. The schematic of this test rig is shown in Fig. 2. The objective here is to measure the temperature drop/gain achieved by the fluids when maneuvering through the heat exchanger.

The non-reactivity and compatibility of water with the exchanger material instigated its choice as the working fluid. The test flow rates are deliberately kept low in the range of $100 - 270ml/min$, to avoid mechanical failure of the thin separating walls under the pressure of fluid flow. Two 'Cole-Parmer® Polystat® Cooling/Heating Circulating Baths', commonly known as chillers, circulate water through the exchanger test

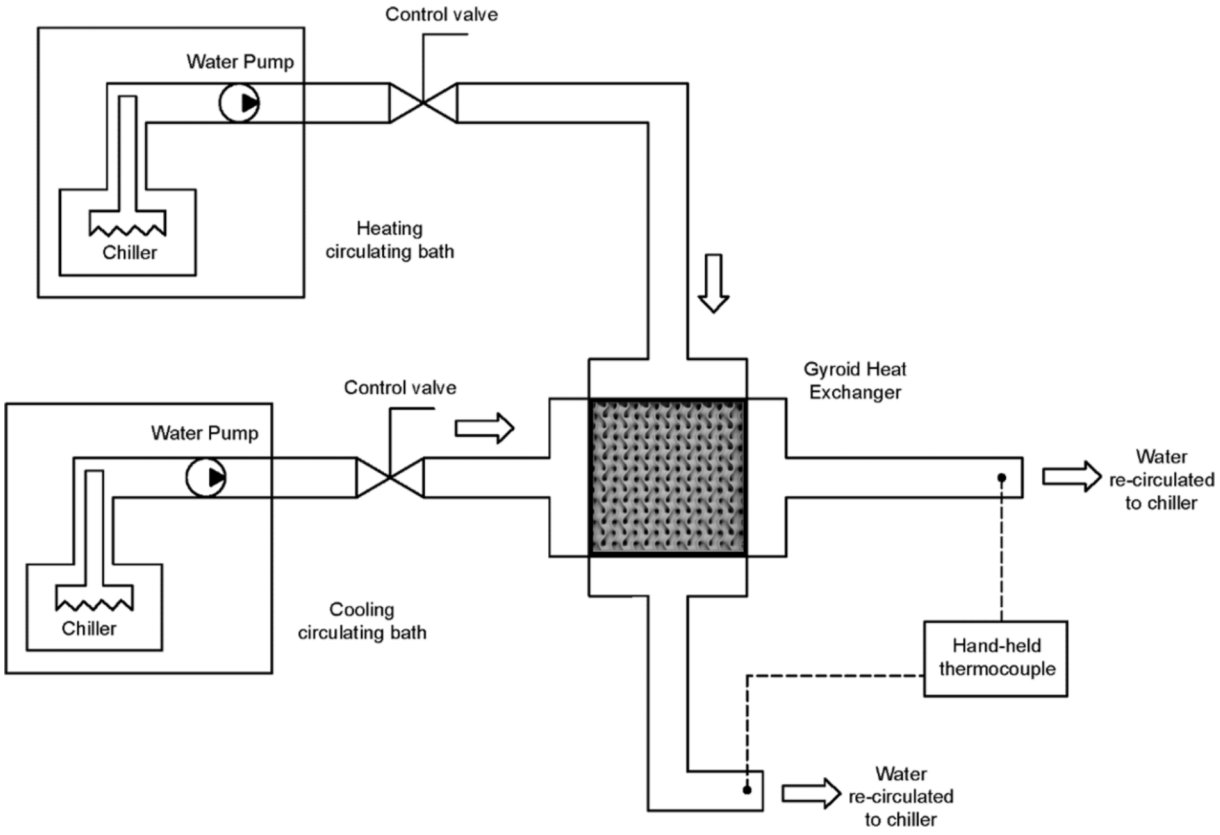

Fig. 2. Schematic view of table-top experimental test-rig for evaluating the heat transfer performance of 3D printed gyroid heat exchanger.

circuit. Water is pumped by both the chillers each discharging it at set temperature of 60 °C and 20 °C respectively. The glass transition temperature of PlasGray polymer (84 °C) chosen for the exchanger governs the maximum permissible temperature within the heat exchanger. Manual valves placed between the chillers and the exchanger hot fluid and cold fluid inlet headers facilitate the control of fluid flow rate. The temperature difference between the hot and cold fluid enables heat exchange between fluids through the thin separating wall. The hot fluid (after losing heat) along with the cold fluid (after gaining heat) exit the heat exchanger where the flow rates are evaluated using conventional beaker-timer measurement technique. The volumetric flow rate is recorded by the volume of fluid collected in a beaker for 1 min. This exercise is followed three times during each test at an interval of few minutes and an average of three recordings is taken as the volumetric flow rate of the hot/cold fluid. Hand-held thermocouple digitally displays the temperature of the fluids at the exit. Although 2*mm* thick external walls of the heat exchanger provide thermal insulation to prevent the ambient heat in-leak, additional flexible foam thermal insulation is added to the exterior surface of the exchanger. Tests are conducted at different volumetric flow rates and the data is collected under steady-state conditions.

Prior to fabrication of the heat exchanger, some of the key thermal properties of 'PlasGRAY v2′ photopolymer is quantitatively evaluated by 'Hot Disk Thermal Constant Analyzer'. The thermal conductivity and the specific heat at constant temperature of the polymer material is found to be $0.18 W/m^2K$ and $2450 J/kgK$ respectively. As per the manufacturer's data [70], glass transition temperature of this polymer is 84 °C and its density is $1181 \mathrm{kg/m^3}$. Error analysis associated with the experimental data is calculated by the root-sum-square method of Moffat [71] given by the equation,

$$\delta R = \left[\sum_{i=1}^{n} \left(\frac{\partial R}{\partial x_i} \delta x_i \right)^2 \right]^{1/2} \quad (1)$$

The uncertainty in measurement of temperature is ±0.5 °C and that of volumetric flow rate is ±15%. The relatively large uncertainty in volumetric flow rate is associated with the measuring beaker (with a least count of 20 ml) and the stopwatch (with a least count of 1 s) employed.

v. Element modelling. In addition to the experimental evaluation of the exchanger performance, preliminary finite element (FE) analysis is conducted to corroborate FE results with the experimental results. FE analysis provides insight into the temperature and the fluid fields within the gyroid architecture which may be challenging to capture experimentally. The FE analysis is conducted using the finite element analysis software *COMSOL Multiphysics*®. Its 'Conjugate Heat Transfer, Laminar Flow' module assists in simulating the heat transfer and fluid flow characteristics of the gyroid architecture. A gyroid unit-cell (the smallest repeating element of gyroid heat exchanger) is imported into *COMSOL* using its geometry interface (Fig. 3a). Two fluid flow channels are created as can be distinguished by green and blue color shown in Fig. 3b representing the hot and cold fluids respectively. The solid domain is specified with the material properties identified for the exchanger material PlasGRAY v2 while the fluid domain is chosen as water with its properties extracted from the in-built material library. Referring to the geometric model shown in Fig. 3b, hot fluid flows along $+y$ axis and the cold fluid flows along $-z$ axis. Instead of periodic boundaries, solid walls perpendicular to the flow directions were considered. Corresponding to the actual experimental mass flow rates (assuming equal flow rate through the channels), $1/(7*7)$ th of its value is taken as the numerical mass flow rate for both hot and cold fluids. However, fluid inlet temperatures for the simulation are same as those of experimentally measured values. A spatially uniform inlet velocity and temperature conditions are considered at the entry of both hot and cold fluids in the FE simulation. Exit boundaries are defined while the remaining surfaces are imposed with thermal insulation boundary condition. Free tetrahedral elements are found to aptly mesh the complex gyroid

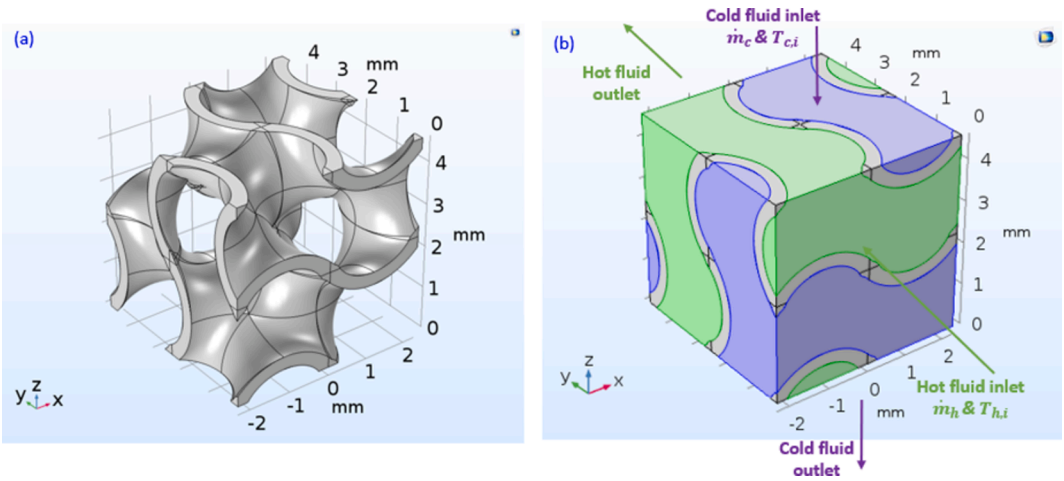

Fig. 3. *COMSOL Multiphysics* environment for heat transfer and fluid flow simulation (a) imported CAD gyroid unit-cell of size $4.6mm \times 4.6mm \times 4.6mm$ and wall thickness of $300\mu m$ (b) physical model depicting imposed boundary conditions.

architecture. GMRES stationary solver simulates the steady-state conditions within the unit-cell of gyroid heat exchanger. Simulations were conducted for all the experimental data points measured with each computation requiring approximately 9 h.

3. Results & discussion

The experimental and numerical results of the additively manufactured gyroid compact heat exchanger are presented in this section. At the start of the experimentation, cold run trials are conducted to check for leaks once again. The working fluid (water) is made to pass through only one side of the exchanger and no outflow of fluid is observed though the other side thereby confirming a leak-free heat exchanger. Water initially gushes out the trapped air bubbles within the exchanger. It takes a while for the flow to become bubble-free and stable. It is interesting to observe the contours of air bubbles thereby giving a sense of disturbance imparted by the gyroid structure to the fluid flow. This disturbance enhances the heat transfer rate owing to perhaps the geometry-imposed localized fluid disturbance.

The entry and exit temperatures of both hot and cold fluids measured experimentally are graphically presented in Fig. 4a for four different flow rates. The abscissa represents the tests conducted and the test number corresponds to a particular pair of flow rates of the hot and cold fluids, $\dot{V}_{hot}$ and $\dot{V}_{cold}$ respectively. A temperature drop of $13-20\ ^{\circ}C$ for the hot fluid from the inlet temperature of $60\ ^{\circ}C$ is noted. Dissimilar flow rates on both sides result in a temperature gain of $14-10\ ^{\circ}C$ for the cold fluid having an inlet temperature of $20\ ^{\circ}C$. Change in fluid temperature is more pronounced at lower flow rates owing to higher fluid residence time. Fig. 4b gives the heat transfer rates of the two fluid streams as they thermally interact with each other. The heat transfer rate for the hot fluid (Q_h) and the heat transfer-rate for the cold fluid (Q_c) are evaluated using the Newton's law of cooling [72], given by:

$$Q_h = \dot{m}_h C_{p,h}\left(T_{h,i} - T_{h,o}\right) \tag{2}$$

$$Q_c = \dot{m}_c C_{p,c}\left(T_{c,o} - T_{c,i}\right) \tag{3}$$

The experimental uncertainty, based on the uncertainty in measurement of volumetric flow rate and temperature, is about $\pm 17\%$ for Q_h and $\pm 14\%$ for Q_c. The average rate of heat transfer, approximately in the range of $120-220W$, enhances with increase in volumetric flow rates. The divergence of Q_h and Q_c, although within the experimental uncertainty, is observed to increase at higher flow rates. This may be associated with higher ambient heat loss at larger mass flow rates.

The three-dimensional distribution of temperature and pressure obtained from FE simulation of a single gyroid unit-cell is depicted in Fig. 5. Results shown are for the data corresponding to the first experimental data point (test number 1). Mapping of the experimental and numerical data is done by keeping identical mass flow rates of fluid through each unit-cell. In other words, simulations are conducted at 1/(7*7) th of the experimental flow rate. Just across the unit-cell size of $4.6mm$, the gyroid architecture is able to impart a hot fluid temperature drop of $4.6\ ^{\circ}C$ and a cold fluid temperature gain of $3.7\ ^{\circ}C$ corresponding

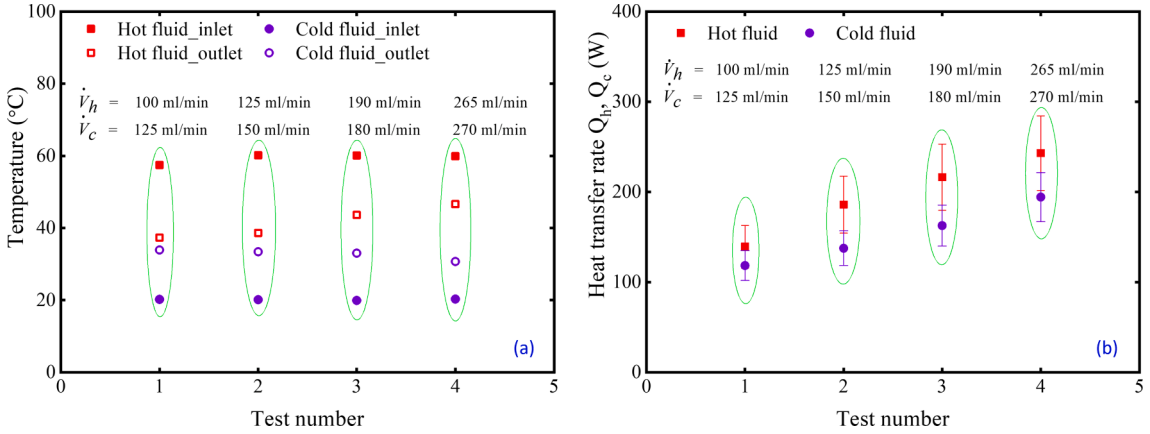

Fig. 4. Experimentally measured (a) inlet and exit temperatures of hot and cold fluid in the gyroid heat exchanger (b) rate of heat transfer between hot and cold fluid.

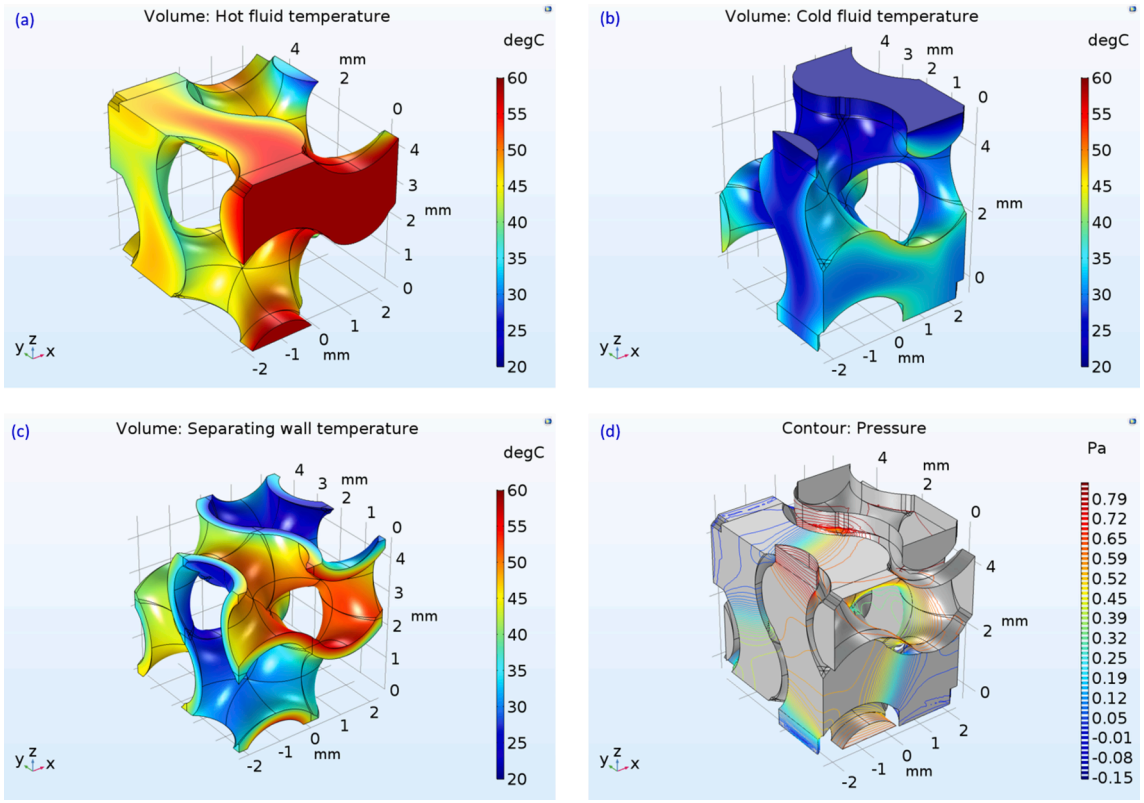

Fig. 5. Simulated thermal *iso*-surface for (a) hot fluid (b) cold fluid (c) separating wall and (d) pressure contours corresponding to experimental test number 1.

to mass flow rates of $3.4 \times 10^{-05} kg/s$ and $4.2 \times 10^{-05} kg/s$ respectively. This observation motivates us to further explore the effectiveness of the gyroid lattice heat exchanger. The temperature distribution in hot fluid, cold fluid and in the $300\mu m$ gyroid wall across the unit cell are shown in Fig. 5a, 5b and 5c respectively.

For the singule gyroid unit cell, the pressure drop is not considerable as evident from Fig. 5d. Extrapolating the simulated pressure drop over the entire length of the fabricated heat exchanger is also found to be insignificant. Consequently, efforts to measure the same pressure drop experimentally were not made.

Comparison of the experimentally and numerically calculated overall heat transfer coefficient results for microarchitected gyroid heat exchanger is depicted in Fig. 6. The overall heat transfer coefficient U is given in the left-hand y-axis against the Reynolds number Re_h corresponding to the hot fluid. Overall, the heat transfer coefficient is evaluated using,

$$U = Q_{avg}/(A_s \Delta T_{LMTD}) \tag{4}$$

where Q_{avg} is the average of Q_h and Q_c

$$\Delta T_{LMTD} = \frac{(T_{h,i} - T_{c,o}) - (T_{h,o} - T_{c,i})}{\ln \frac{(T_{h,i} - T_{c,o})}{(T_{h,o} - T_{c,i})}} \tag{5}$$

and the Reynolds number corresponding to the hot fluid is given by,

$$Re_h = \left(\frac{\dot{m}_h}{A_c}\right) \frac{D_h}{\mu} \tag{6}$$

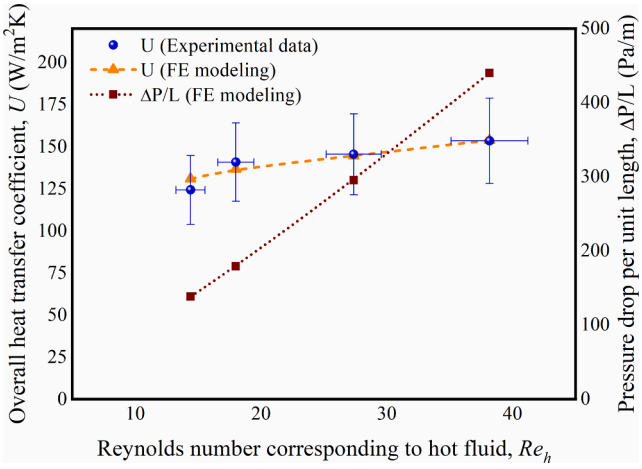

Fig. 6. Experimentally measured and numerically simulated overall heat transfer coefficient (LHS Y-axis) as a function of Reynolds number. Predicted pressure drop per unit length (RHS Y-axis) against the Reynolds number.

Choice of these parameters permits effect of size scaling to be neglected since simulation is conducted for a single unit-cell while experimentation is done on an array of unit cells.

Corresponding to the hot fluid Reynolds number Re_h of 10 –40, overall heat transfer coefficient of the designed gyroid compact heat exchanger is in the range of $120 - 160 W/m^2K$. It is evident from Fig. 6 that finite element model accurately captures the measured data. Additionally, the predicted pressure drop per unit length scale for the actual heat exchanger dimensions is depicted in the same graph (see RHS vertical axis) against Reynolds number.

Performance maps. This section showcases the performance of our AM-enable microarchitected gyroid heat exchanger in comparison to that of several other exchangers reported in the literature [16,38,39,48,49,52,73] in terms of heat exchanger effectiveness $\varepsilon = \frac{\left(\dot{m}_h C_{p,h}(T_{h,i} - T_{h,0}) + \dot{m}_c C_{p,c}(T_{c,o} - T_{c,i})\right)/2}{(\dot{m}C_p)_{min}(T_{h,i} - T_{c,i})}$ and *volumetric* heat transfer coefficient $Q_{avg}/(V\Delta T_{LMTD})$ in Fig. 7a–7c. The effectiveness in Fig. 7a is based on cold side heat transfer rate while in Fig. 7b the average of hot and cold side effectiveness is presented (as similar method has been

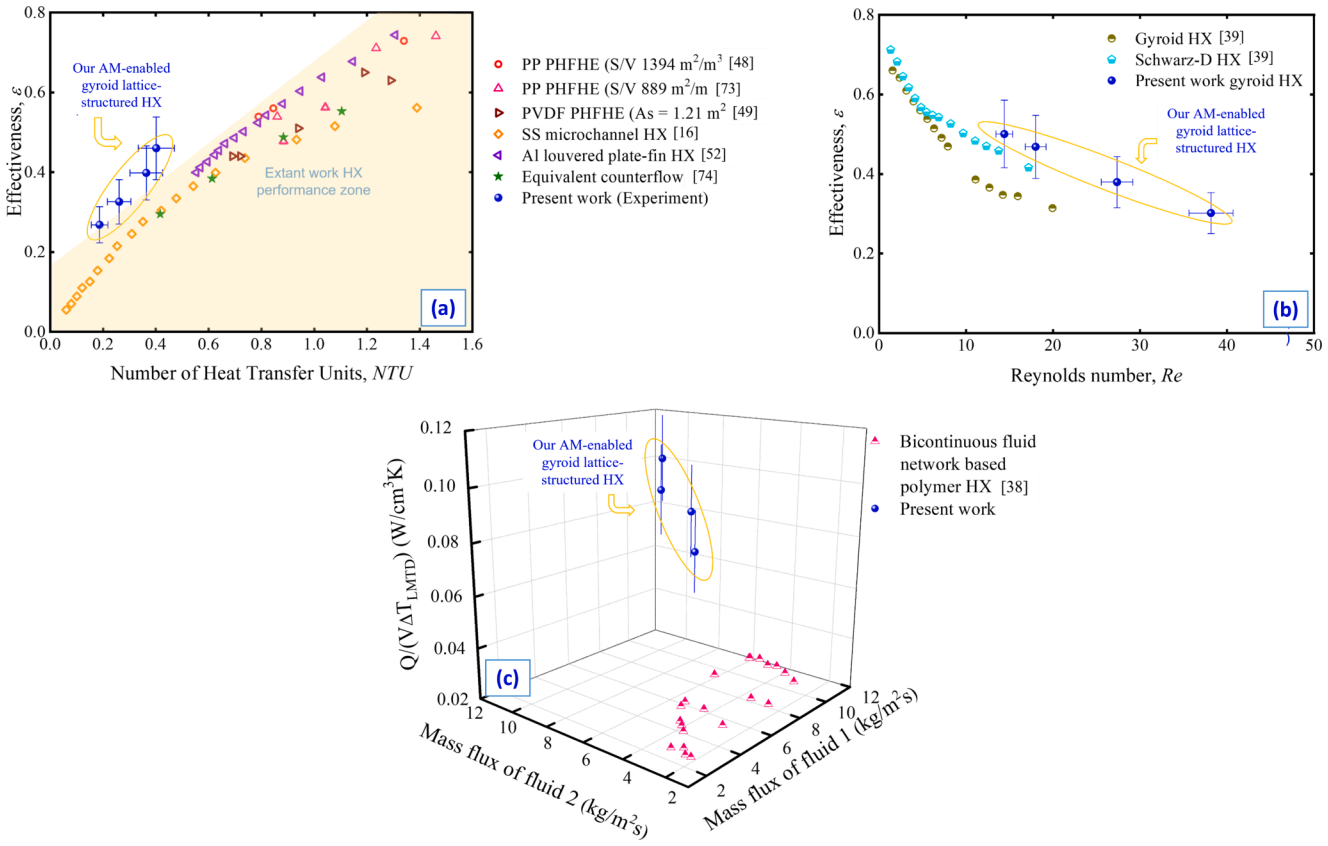

Fig. 7. Comparison of the performance of AM-enabled heat exchanger in terms of (a) effectiveness against number of heat transfer units (b) effectiveness against Reynolds number and (c) volumetric heat transfer coefficient against mass flux of exchanger fluids.

followed in the extant works with which the comparison has been made).

It is interesting to note from Fig. 7a that, under similar flow conditions, the gyroid exchanger devised here supersedes the performance of other polymer, metallic, lattice-based, highly compact and non-compact heat exchangers in low number of transfer units (NTU) range with $NTU = UA_s/(\dot{m}C_p)_{min}$. The high surface area density of the TPMS lattice structure particularly arising at the microscale, enhances the heat transfer performance of such microarchitected gyroid heat exchanger. Revisiting Fig. 5, it can be seen that the surface curvature of TPMS geometry constantly changes along the fluid flow direction. The locally imparted turbulence induces fluid tortuosity (observed during experimentation as well), leading to further improved performance of the heat exchanger. Additionally, performance of our gyroid heat exchanger is compared particularly with counter-flow heat exchanger which thermodynamically has the most efficient flow arrangement [74]. An enhancement in effectiveness of nearly 55%, corresponding to *NTU* of 0.4, is achieved by the microarchitected gyroid heat exchanger (see Fig. 7a). The equivalent counter-flow heat exchanger has a rectangular cross-sectional duct of $b/a = 8.0$ and the same inlet flow area and separating wall thickness as well as the same heat transfer area as that of the gyroid heat exchanger. An addition to the number of advantages already mentioned now includes superior effectiveness at just 1/10th the size of an equivalent counter-flow heat exchanger.

When compared to similar size additively manufactured TPMS heat exchangers [38], the devised gyroid exchanger reflects higher effectiveness in low Reynold number range as shown in Fig. 7b. For instance, at $Re = 17$, the current configuration of gyroid exchanger shows 30% higher effectiveness than that reported in [38]. It confirms that AM-enabled tailoring of geometrical parameters can dramatically enhance the performance limits. This can also be seen from the 3D graph of Fig. 7c wherein the volumetric heat transfer coefficient of the present exchanger configuration exceeds the cross-flow exchanger based on dense micro-lattice of hollow tubes in the same range of fluid mass fluxes [39].

4. Conclusions

In this study, the design, additive manufacturing and the heat exchange characteristics of microarchitected gyroid lattice heat exchanger have been demonstrated. The thermal performance of TPMS-based heat exchanger was experimentally measured. Finite Element analysis of gyroid unit-cell with solid walls perpendicular to the flow directions and spatially uniform inlet velocity and temperature conditions of both hot and cold fluids was also conducted to numerically predict the thermo-hydraulic characteristics. The conclusions drawn from this study are enlisted as follows:

- Additive manufacturing technology facilitates the fabrication of the TPMS-based microarchitected heat exchanger along with the headers as single unit – a feat difficult to achieve by conventional techniques. X-ray computed tomography analysis confirms a defect-free 3D printed compact heat exchanger with a surface area density of $670 m^2/m^3$.
- The microarchitected gyroid lattice heat exchanger core with an overall dimension of 32.2 mm × 32.2 mm × 32.2 mm exhibits a temperature gain/drop of 10 −20 °C over the volumetric flow rates of $100 - 270 ml/min$, leading to an overall heat transfer coefficient of $120 - 160 W/m^2K$ for hot fluid Reynolds number Re_h in the range of 10 −40.
- Despite relatively high uncertainty in the measurement variables, the gyroid lattice heat exchanger showcases higher effectiveness as compared to previously reported additively manufactured, non-additively manufactured, polymer, metallic, lattice-based, highly

compact and non-compact heat exchangers in low NTU range. The superior performance of our AM-enabled gyroid lattice heat exchanger is attributed to its smooth topology and large surface area density.

- The additively manufactured gyroid-lattice heat exchanger exhibits a 55 % increase in effectiveness in comparison to a thermodynamically equivalent, most-efficient, counter-flow heat exchanger at 1/10th of its size.
- Finite Element analysis of the gyroid unit-cell with periodic boundary and other appropriate conditions that exactly mimic the experiments would require a subsequent study to gain a deeper insight into the heat transfer and fluid flow characteristics of AM-enabled gyroid lattice heat exchangers.

Declaration of Competing Interest

The authors declare that they have no known competing financial interests or personal relationships that could have appeared to influence the work reported in this paper.

Acknowledgement

Authors would like to thank to Abu Dhabi National Oil Company (ADNOC) for providing the research grant (Award No: EX2016-000010). S. Kumar would like to thank the University of Glasgow for the start-up grant [Award No: 144690-01].

References

[1] E. Dugbenoo, M.F. Arif, B.L. Wardle, S. Kumar, Enhanced bonding via additive manufacturing-enabled surface tailoring of 3D printed continuous-fiber composites, Adv. Eng. Mater. 20 (12) (2018) 1800691, https://doi.org/10.1002/adem.v20.1210.1002/adem.201800691.
[2] J.J. Andrew, J. Ubaid, F. Hafeez, A. Schiffer, S. Kumar, Impact performance enhancement of honeycombs through additive manufacturing-enabled geometrical tailoring, Int. J. Impact Eng. 134 (2019), 103360.
[3] S. Yun, J. Kwon, D. Lee, H.H. Shin, Y. Kim, Heat transfer and stress characteristics of additive manufactured FCCZ lattice channel using thermal fluid-structure interaction model, Int. J. Heat Mass Transf. 149 (2020), 119187.
[4] H.J. O'Connor, A.N. Dickson, D.P. Dowling, Evaluation of the mechanical performance of polymer parts fabricated using a production scale multi jet fusion printing process, Addit. Manuf. 22 (2018) 381–387.
[5] S. Kumar, J. Ubaid, R. Abishera, A. Schiffer, V.S. Deshpande, Tunable energy absorption characteristics of architected honeycombs enabled via additive manufacturing, ACS Appl. Mater. Interfaces 11 (45) (2019) 42549–42560.
[6] J. Schneider, S. Kumar, Multiscale characterization and constitutive parameters identification of polyamide (PA12) processed via selective laser sintering, Polym. Test. 86 (2020), 106357.
[7] Z. Ma, D.Z. Zhang, F. Liu, J. Jiang, M. Zhao, T. Zhang, Lattice structures of Cu-Cr-Zr copper alloy by selective laser melting: Microstructures, mechanical properties and energy absorption, Mater. Des. 187 (2020), 108406.
[8] P. Wang, J. Song, M.L.S. Nai, J. Wei, Experimental analysis of additively manufactured component and design guidelines for lightweight structures: A case study using electron beam melting, Addit. Manuf. 33 (2020), 101088.
[9] J. Bauer, L. Meza, T.A. Schaedler, R. Schwaiger, X. Zheng, L. Valdevit, Nanolattices: An Emerging Class of Mechanical Metamaterials, Adv. Mater. 29 (40) (2017) 1701850.
[10] A. Vyatskikh, S. Delalande, A. Kudo, X. Zhang, C.M. Portela, J.R. Greer, Additive manufacturing of 3D nano-architected metals, Nat. Commun. 9 (2018) 593.
[11] U. Scheithauer, R. Kordaß, K. Noack, M.F. Eichenauer, M. Hartmann, J. Abel, G. Ganzer, D. Lordick, Potentials and challenges of additive manufacturing technologies for heat exchanger, in: L.C. Gomez, V.M.V. Flores (Eds.), Advances in Heat Exchangers, IntechOpen, 2019, pp. 41–61.
[12] D. Jafari, W.W. Wits, The utilization of selective laser melting technology on heat transfer devices for thermal energy conversion applications: A review, Renew. Sustain. Energy Rev. 91 (2018) 420–442.
[13] S.M. Thompson, Z.S. Aspin, N. Shamsaei, A. Elwany, L. Bian, Additive manufacturing of heat exchangers: A case study on a multi-layered Ti–6Al–4V oscillating heat pipe, Addit. Manuf. 8 (2015) 163–174.
[14] M.A. Arie, A.H. Shooshtari, M.M. Ohadi, Experimental characterization of an additively manufactured heat exchanger for dry cooling of power plants, Appl. Therm. Eng. 129 (2018) 187–198.
[15] X. Zhang, R. Tiwari, A.H. Shooshtari, M.M. Ohadi, An additively manufactured metallic manifold-microchannel heat exchanger for high temperature applications, Appl. Therm. Eng. 143 (2018) 899–908.
[16] Bichnevicius M, Saltzman D, Lynch S, comparison of louvered plate-fin heat exchangers made via additive manufacturing, Proceedings of the ASME 2018 International Mechanical Engineering Congress and Exposition, November 9-15, 2018, Pittsburgh, PA, USA, IMECE2018-87941.
[17] D. Saltzman, M. Bichnevicius, S. Lynch, T.W. Simpson, E.W. Reutzel, C. Dickman, R. Martukanitz, Design and evaluation of an additively manufactured aircraft heat exchanger, Appl. Therm. Eng. 138 (2018) 254–263.
[18] K. Navickaitė, A. Mocerino, L. Cattani, F. Bozzoli, C. Bahl, K. Liltrop, X. Zhang, K. Engelbrecht, Enhanced heat transfer in tubes based on vascular heat exchangers in fish: Experimental investigation, Int. J. Heat Mass Transf. 137 (2019) 192–203.
[19] G. Huang, Y. Zhu, Z.-Y. Liao, Z. Huang, P.-X. Jiang, Transpiration cooling with bio-inspired structured surfaces, Bioinspiration Biomimetics 15 (3) (2020) 036016, https://doi.org/10.1088/1748-3190/ab6bdf.
[20] S. Unger, M. Beyer, S. Gruber, R. Willner, U. Hampel, Experimental study on the air-side thermal-flow performance of additively manufactured heat exchangers with novel fin designs, Int. J. Therm. Sci. 146 (2019), 106074.
[21] T.A. Schaedler, A.J. Jacobsen, A. Torrents, A.E. Sorensen, J. Lian, J.R. Greer, L. Valdevit, W.B. Carter, Ultralight metallic microlattices, Science 334 (6058) (2011) 962–965.
[22] T.A. Schaedler, W.B. Carter, Architected Cellular Materials, Annu. Rev. Mater. Res. 46 (1) (2016) 187–210.
[23] X. Zheng, H. Lee, T.H. Weisgraber, M. Shusteff, J. DeOtte, E.B. Duoss, J.D. Kuntz, M.M. Biener, Q.i. Ge, J.A. Jackson, S.O. Kucheyev, N.X. Fang, C.M. Spadaccini, Ultralight, ultrastiff mechanical metamaterials, Science 344 (6190) (2014) 1373–1377.
[24] T. Tancogne-Dejean, M. Diamantopoulou, M.B. Gorji, C. Bonatti, D. Mohr, 3D plate-lattices: An emerging class of low-density metamaterial exhibiting optimal isotropic stiffness, Adv. Mater. 30 (45) (2018) 1803334.
[25] Kumar S, Tan S, Zheng L, Kochmann DM, Inverse-designed spinodoid metamaterials, npj Computational Materials 6 (2020) 73.
[26] H. Cui, R. Hensleigh, D. Yao, D. Maurya, P. Kumar, M.G. Kang, S. Priya, X.(. Zheng, Three-dimensional printing of piezoelectric materials with designed anisotropy and directional response, Nat. Mater. 18 (3) (2019) 234–241.
[27] Jefferson JJ, Alhashmi H, Schiffer A, Kumar S, Deshpande V, Energy absorption and self-sensing performance of 3D printed CF/PEEK cellular composites, Materials and Design, In Review (2021).
[28] P. Verma, T. Bansala, S.S. Chauhan, D. Kumar, S. Deveci, S. Kumar, Electromagnetic interference shielding performance of carbon nanostructure reinforced, 3D printed polymer composites, J. Mater. Sci. 56 (20) (2021) 11769–11788.
[29] C.M. Soukoulis, M. Wegener, Optical metamaterials—more bulky and less lossy, Science 330 (6011) (2010) 1633–1634.
[30] V. Gupta, F. Alam, P. Verma, A.M. Kannan, S. Kumar, Additive manufacturing enabled, microarchitected, hierarchically porous polylactic-acid/Lithium iron phosphate/carbon nanotube nanocomposite electrodes for high performance Li, J. Power Sources 494 (2021), 229625.
[31] S.R. Sklan, B. Li, Thermal metamaterials: functions and prospects, Natl. Sci. Rev. 5 (2) (2018) 138–141.
[32] A. Mirabolghasemi, A.H. Akbarzadeh, D. Rodrigue, D. Therriault, Thermal conductivity of architected cellular metamaterials, Acta Mater. 174 (2019) 61–80.
[33] T. Dixit, P. Nithiarasu, S. Kumar, Numerical evaluation of additively manufactured lattice architectures for heat sink applications, Int. J. Therm. Sci. 159 (2021), 106607.
[34] M. Ashby, Designing architectured materials, Scr. Mater. 68 (1) (2013) 4–7.
[35] Y. Brechet, J.D. Embury, Architectured materials: Expanding materials space, Scr. Mater. 68 (1) (2013) 1–3.
[36] Kim T, Hodson HP, Lu TJ, Pressure loss and heat transfer mechanisms in a lattice-frame structured heat exchanger, Proceedings of the Institution of Mechanical Engineers Part C: Journal of Mechanical Engineering Science 218 (11) (2004) 1321-1336.
[37] K.N. Son, J.A. Weibel, V. Kumaresan, S.V. Garimella, Design of multifunctional lattice-frame materials for compact heat exchangers, Int. J. Heat Mass Transf. 115 (2017) 619–629.
[38] C.S. Roper, R.C. Schubert, K.J. Maloney, D. Page, C.J. Ro, S.S. Yang, A.J. Jacobsen, Scalable 3D bicontinuous fluid networks: Polymer heat exchangers toward artificial organs, Adv. Mater. 27 (15) (2015) 2479–2484.
[39] T. Femmer, A.J.C. Kuehne, M. Wessling, Estimation of the structure dependent performance of 3-D rapid prototyped membranes, Chem. Eng. J. 273 (2015) 438–445.
[40] K.K. Wong, K.C. Leong, Saturated pool boiling enhancement using porous lattice structures produced by Selective Laser Melting, Int. J. Heat Mass Transf. 121 (2018) 46–63.
[41] M. Pelanconi, M. Barbato, S. Zavattoni, G.L. Vignoles, A. Ortona, Thermal design, optimization and additive manufacturing of ceramic regular structures to maximize the radiative heat transfer, Mater. Des. 163 (2019), 107539.
[42] A.R.J. Hussain, A.A. Alahyari, S.A. Eastman, C. Thibaud-Erkey, S. Johnston, M. J. Sobkowicz, Review of polymers for heat exchanger applications: Factors concerning thermal conductivity, Appl. Therm. Eng. 113 (2017) 1118–1127.
[43] C. T'Joen, Y. Park, Q. Wang, A. Sommers, X. Han, A. Jacobi, A review on polymer heat exchangers for HVAC&R applications, Int. J. Refrig 32 (2009) 767–779.
[44] Z. Han, A. Fina, Thermal conductivity of carbon nanotubes and their polymer nanocomposites: A review, Prog. Polym. Sci. 36 (7) (2011) 914–944.
[45] J.G. Cevallos, A.E. Bergles, A. Bar-Cohen, P. Rodgers, S.K. Gupta, Polymer Heat Exchangers—History, Opportunities, and Challenges, Heat Transfer Eng. 33 (13) (2012) 1075–1093.
[46] S.L. Gómez Aláez, P. Bombarda, C.M. Invernizzi, P. Iora, P. Silva, Evaluation of ORC modules performance adopting commercial plastic heat exchangers, Appl. Energy 154 (2015) 882–890.

[47] X. Chen, Y. Su, D. Reay, S. Riffat, Recent research developments in polymer heat exchangers – A review, Renew. Sustain. Energy Rev. 60 (2016) 1367–1386.
[48] D.M. Zarkadas, K.K. Sirkar, Polymeric hollow fiber heat exchangers: An alternative for lower temperature applications, Ind. Eng. Chem. Res. 43 (2004) 8093–8106.
[49] X. Chen, Y. Su, D. Aydin, D. Reay, R. Law, S. Riffat, Experimental investigations of polymer hollow fibre heat exchangers for building heat recovery application, Energy Build. 125 (2016) 99–108.
[50] I. Krásný, I. Astrouski, M. Raudenský, Polymeric hollow fiber heat exchanger as an automotive radiator, Appl. Therm. Eng. 108 (2016) 798–803.
[51] M. Raudenský, I. Astrouski, M. Dohnal, Intensification of heat transfer of polymeric hollow fiber heat exchangers by chaotisation, Appl. Therm. Eng. 113 (2017) 632–638.
[52] S. Song, H. Shan, J. Liu, B. Li, Heat transfer study of PVDF hollow fiber heat exchanger for desalination process, Desalination 446 (2018) 1–11.
[53] L. Zaheed, R. Jachuck, Performance of a square, cross-corrugated, polymer film, compact, heat-exchanger with potential application in fuel cells, J. Power Sources 140 (2) (2005) 304–310.
[54] M.A. Arie, A.H. Shooshtari, R. Tiwari, S.V. Dessiatoun, M.M. Ohadi, J.M. Pearce, Experimental characterization of heat transfer in an additively manufactured polymer heat exchanger, Appl. Therm. Eng. 113 (2017) 575–584.
[55] L. Chen, Z. Li, Z.-Y. Guo, Experimental investigation of plastic finned-tube heat exchangers, with emphasis on material thermal conductivity, Exp. Therm Fluid Sci. 33 (5) (2009) 922–928.
[56] S. Ma, Q. Tang, X. Han, Q. Feng, J. Song, R. Setchi, Y. Liu, Y. Liu, A. Goulas, D. S. Engstrøm, Y.Y. Tse, N. Zhen, Manufacturability, mechanical properties, mass-transport properties and biocompatibility of triply periodic minimal surface (TPMS) porous scaffolds fabricated by selective laser melting, Mater. Des. 195 (2020), 109034.
[57] S. Yu, J. Sun, J. Bai, Investigation of functionally graded TPMS structures fabricated by additive manufacturing, Mater. Des. 182 (2019), 108021.
[58] A.A. Zadpoor, Additively manufactured porous metallic biomaterials, J. Mater. Chem. B 7 (26) (2019) 4088–4117.
[59] S. Catchpole-Smith, R.R.J. Selo, A.W. Davis, I.A. Ashcroft, C.J. Tuck, A. Clare, Thermal conductivity of TPMS lattice structures manufactured via laser powder bed fusion, Addit. Manuf. 30 (2019), 100846.
[60] X.C. Ye, X.C. Lin, J.Y. Xiong, H.H. Wu, G.W. Zhao, D. Fang, Electrical properties of 3D printed graphite cellular lattice structures with triply periodic minimal surface architectures, Mater. Res. Express 6 (2019), 125609.
[61] D.A. Clarke, F. Dolamore, C.J. Fee, P. Galvosas, D.J. Holland, Investigation of flow through triply periodic minimal surface-structured, porous media using MRI and CFD, Chem. Eng. Sci. 231 (2021), 116264.
[62] Peng H, Gao F, Hu W, Design, modeling and characterization of triply periodic minimal surface heat exchangers with additive manufacturing, Proceedings of the 30th Annual International Solid Freeform Fabrication Symposium, August 12-19, 2019, Texas USA.
[63] W. Li, G. Yu, Z. Yu, Bioinspired heat exchangers based on triply periodic minimal surfaces for supercritical CO2 cycles, Appl. Therm. Eng. 179 (2020), 115686.
[64] J. Kim, D.J. Yoo, 3D printed compact heat exchangers with mathematically defined core structures, J. Comput. Des. Eng. 7 (4) (2020) 527–550.
[65] S.D. Nath, S. Nilufar, An overview of additive manufacturing of polymers and associated composites, Polymers 12 (2020) 2719.
[66] I. Kaur, P. Singh, Critical evaluation of additively manufactured metal lattices for viability in advanced heat exchangers, Int. J. Heat Mass Transf. 168 (2021), 120858.
[67] P.J.F. Gandy, J. Klinowski, Exact computation of the triply periodic G (‘Gyroid’) minimal surface, Chem. Phys. Lett. 321 (5-6) (2000) 363–371.
[68] L. Han, S. Che, An overview of materials with triply periodic minimal surfaces and related geometry: From biological structures to self-assembled systems, Adv. Mater. 30 (2018) 1705708.
[69] S.B.G. Blanquer, M. Werner, M. Hannula, S. Sharifi, G.P.R. Lajoinie, D. Eglin, J. Hyttinen, A.A. Poot, D.W. Grijpma, Surface curvature in triply-periodic minimal surface architectures as a distinct design parameter in preparing advanced tissue engineering scaffolds, Biofabrication 9 (2017), 025001.
[70] ASIGA 2021, accessed February 27 2022 <https://www.asiga.com/media/main/files/materials/Asiga%20Material%20Handbook%20-%20Jewelry%20en_US.pdf>.
[71] R.J. Moffat, Describing the uncertainties in experimental results, Exp. Therm Fluid Sci. 1 (1988) 3–17.
[72] F.P. Incropera, D.P. Dewitt, Fundamentals of Heat and Mass Transfer, 5th edition, Wiley India, New Delhi, 2010.
[73] N. García-Hernando, A. Acosta-Iborra, U. Ruiz-Rivas, M. Izquierdo, Experimental investigation of fluid flow and heat transfer in a single-phase liquid flow micro-heat exchanger, Int. J. Heat Mass Transf. 52 (2009) 5433–5446.
[74] R.K. Shah, D.P. Sekulic, Fundamentals of Heat Exchanger Design, 1st edition, Wiley India, New Delhi, 2003.
[75] Schoen AH, Infinite periodic minimal surfaces without self-intersections, NASA Technical Note TN D-5541, May 1970.